23rd Australasian Fluid Mechanics Conference - 23AFMC
Sydney, Australia
4 – 8 December 2022
Paper No: AFMC2022-124

An Incident Shock Boundary Condition For Eilmer4

Flynn Hack[1*], Ingo Jahn[1], David Buttsworth[1] and Fabian Zander[1]

[1] Institute for Advanced Engineering and Space Sciences, The University of Southern Queensland, Toowoomba, Queensland 4360
*mailto: flynn.hack@usq.edu.au

Abstract

Small perturbations in the separation velocity of spacecraft components during atmospheric breakup can drastically alter the downstream impact location of surviving components. Shock-body interactions between proximal bodies immediately after separation have been shown to have a large effect on aerodynamic loading and consequently the separation velocity. However, modelling these flow conditions is notoriously complex and computationally expensive. In this work, a new incident shock boundary condition based on the isentropic oblique shock relations, was developed and implemented in the Eilmer4 transient, compressible flow simulation program. This new boundary condition enables efficient numerical investigations of aerodynamic loading due to shock-shock interactions on primitive shapes representative of spacecraft components.

The boundary condition was first validated against results from literature, where the dynamics of a sphere shedding from a ramp in hypersonic flow was investigated in detail. Excluding near wall effects, the incident shock boundary condition matched predicted aerodynamic coefficients to within $\Delta C_L < 0.04$ and $\Delta C_D < 0.03$, using a significantly reduced flow domain. Next, a comparison of sphere trajectories, comparing one-way (loosely) coupled trajectory simulations to two-way coupled simulations from the reduced flow domain was completed, confirming suitability of the numerical approach. By characterising the performance of such an approach, this work provides a solid foundation for investigating the dynamics of more complex components with shock-shock interactions.

1 Introduction

As of June 2022, the NASA Orbital Debris Program Office was reportedly tracking over 20,000 objects in Low Earth Orbit (LEO) (NASA (2022)). With satellite 'mega-constellations', such as SpaceX's Starlink, already accounting for a large portion of these objects, the further deployment of these mega-constellations is expected to drastically increase the number of satellites in LEO.

To mitigate the potential for collisions and unplanned re-entry of hardware, many satellite operators are now required to employ firm end-of-life management plans, which often result in planned de-orbit manoeuvres and atmospheric re-entry. Whether planned or unplanned, atmospheric re-entry introduces large aerodynamic and thermal loads to spacecraft, often leading to structural failure.

During structural failure, spacecraft components break up and separate from the body under complex aerodynamic forces caused by the free-stream flow and interactions with other components. Work from Laurence & Deiterding (2011) has demonstrated these components can experience significantly higher lateral velocities than would otherwise be possible, while Reyhanoglu & Alvarado (2013) has shown that small perturbations in the separation velocity of spacecraft components during atmospheric breakup can drastically alter the downstream impact location of surviving components.

For these reasons, the capability to accurately model the Fluid Structure Interactions (FSI) between spacecraft components in high-speed flows and predict the downstream trajectory of such spacecraft

components is critical to ensure the risk of harm to human life and property is minimised. Two such methods for modelling hypersonic FSI are one-way (loosely) and two-way (tightly) coupled CFD and structural dynamics approaches.

Applied to the dispersion of spacecraft components during atmospheric breakup, one-way coupled models can be generated assuming quasi-steady conditions, where steady state operating points are simulated to obtain aerodynamic forces. The aerodynamic forces can then be tabulated for use in a separate dynamics model, where the structural dynamics can be predicted. Two-way coupled models can be generated by coupling both CFD and the dynamics model in a variety of ways, where aerodynamic forces affect the object's motion, and visa versa. Both approaches have previously been applied to modelling proximal bodies in hypersonic free-flight conditions (Butler et al (2021), Laurence & Deiterding (2011)).

Although one-way coupled trajectory models are computationally cheap, they require a large number of expensive CFD simulations to define aerodynamic forces over the entire flow domain. On the other hand, two-way coupled trajectory models require computationally expensive CFD simulations for a singular trajectory. However, each two-way coupled simulation can model a much wider range of conditions. As such, any improvements on the accuracy and computational cost of CFD techniques applied to these approaches can significantly increase the range of numerical studies conducted.

The aim of the current paper is to report on the development and implementation of an incident-shock boundary condition developed for use within the transient, compressible flow CFD program Eilmer (Gibbons et al (2022), Jacobs & Gollan (2016)). The incident-shock boundary condition provides opportunity to reduce the size of flow domain required to simulate free-flight, hypersonic FSI problems. To achieve this aim, a description of the boundary condition formulation is provided, before the capability is demonstrated through an example problem taken from literature. Specifically, the boundary condition is applied to both one-way and two-way coupled trajectory models of the example problem in order to characterise its accuracy across a variety of applications. Results from both trajectory models are compared to results from literature and recommendations for future work are made.

2 Dual State Boundary Condition

To define a boundary condition which models a shock generated by a proximal body, both the location of the shock and the states either side of the shock must be well defined. The flow properties in these states also vary with spatial coordinates. For developmental simplicity, the boundary condition formulated within this paper was developed for the case where two uniform states (state A and state B) are separated by a planar shock in three dimensions. An illustration of the desired flow outcomes for an example computational mesh is provided in figure 1.

(a) Example computational mesh.

(b) Desired flow-field.

Figure 1. Illustration of the desired outcome for the dual-state boundary condition applied to an example computational grid, with flow going into the page.

To generate the desired flow conditions, a reflected boundary approach was employed, with fluid properties assigned to ghost cells. Inflow and outflow conditions were both treated separately, with an inflow condition occurring for upwind flow outside the computational domain (negative flux for outward pointing face normals). The inflow ghost cell states were determined by the location of the boundary cell centre relative to the location of the state separating plane. For the case where this plane intersects part of the inflow boundary cell, a blend of state A and state B was assigned (denoted state C). The outflow ghost states were assigned using a zeroth order flux extrapolation method, where the boundary cell values were copied to ghost cells. As the flux of upwind fluids is extrapolated downstream for outflows, the condition will only be accurate for flow that is supersonic. Care was taken to ensure supersonic outflow was present in all simulations. An illustration of the dual state boundary condition implementation is provided in figure 2.

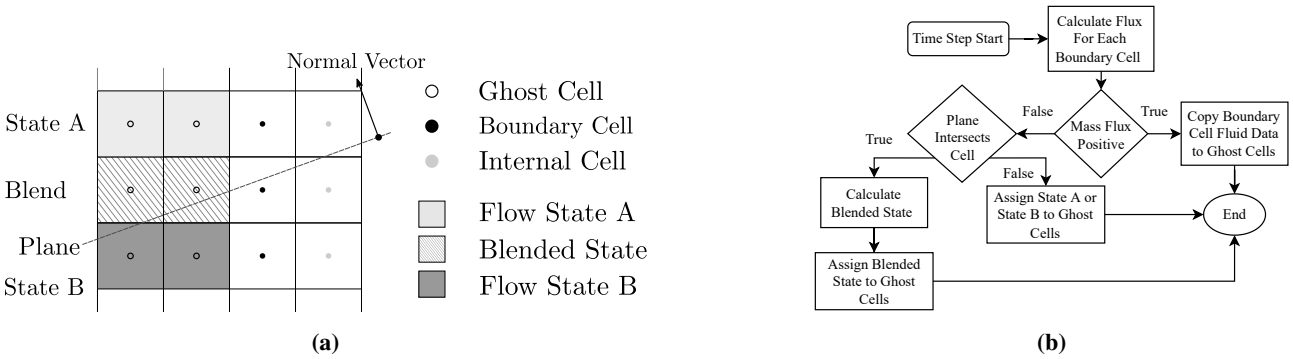

Figure 2. Overview of the dual state boundary condition implementation, with (a) graphically illustrating the process for assigning inflow ghost cell states and (b) outlining the programmatic logic for assigning states to ghost cells, for boundary control surface normals pointing outwards.

State C was formed by calculating properties which ensure mass, momentum and energy flux is conserved through the boundary cell face. With A_a and A_b representing the boundary cell face area state A and B act on respectively, this calculation was defined by equations (1) to (3).

$$\rho A(\tilde{\boldsymbol{u}} \cdot \hat{\boldsymbol{n}})|_c = \rho A(\tilde{\boldsymbol{u}} \cdot \hat{\boldsymbol{n}})|_a + \rho A(\tilde{\boldsymbol{u}} \cdot \hat{\boldsymbol{n}})|_b \tag{1}$$

$$PA|_c + \rho A\tilde{\boldsymbol{u}}(\tilde{\boldsymbol{u}} \cdot \tilde{\boldsymbol{n}})|_c = \rho A\tilde{\boldsymbol{u}}(\tilde{\boldsymbol{u}} \cdot \tilde{\boldsymbol{n}})|_a + \rho A\tilde{\boldsymbol{u}}(\tilde{\boldsymbol{u}} \cdot \tilde{\boldsymbol{n}})|_b + PA|_a + PA|_b \tag{2}$$

$$\rho A(\tilde{\boldsymbol{u}} \cdot \hat{\boldsymbol{n}})h|_c = \rho A(\tilde{\boldsymbol{u}} \cdot \hat{\boldsymbol{n}})h|_a + \rho A(\tilde{\boldsymbol{u}} \cdot \hat{\boldsymbol{n}})h|_b \tag{3}$$

Where ρ is the density, $\hat{\boldsymbol{n}}$ is the cell unit normal vector, P is the static pressure, $\tilde{\boldsymbol{u}}$ is the fluid velocity vector and h is the specific enthalpy. To calculate the six variables required for the blended state (T, ρ, P, u_x, u_y, u_z), a closing equation was required. As this work was validated against simulations representing shock tunnel laboratory conditions with moderate temperatures and pressures, the ideal gas relation was employed for this purpose. Future work will require more sophisticated gas models to model the complex gas dynamics present during free flight in Earth's upper atmosphere.

3 Example Problem

The dual-state boundary condition was applied to a simple, sphere-ramp problem in supersonic flow. The fundamental dynamics of this problem has previously been investigated in detail Butler et al (2021), for the purpose of better understanding particulate shedding from the leading edge of hypersonic wings during flight. Although simplified, this problem greatly reduces the development complexity and allows for validation against previous studies. The sphere-ramp flow problem is illustrated in figure 3.

Assuming a sharp ramp of angle θ, the sphere encounters an oblique incident shock of angle β, which separates two flow states (the free-stream flow and shock processed flow). By taking these

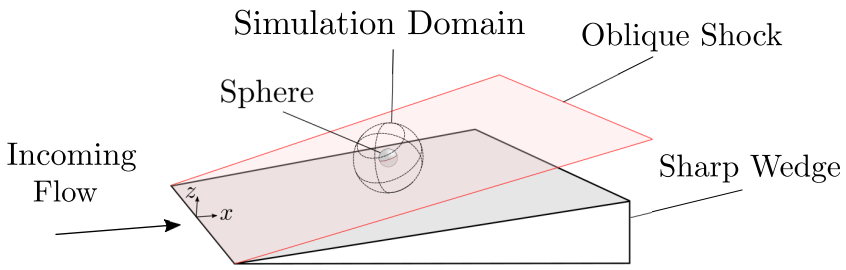

Figure 3. Sphere with oblique incident shock generated from supersonic flow over a sharp ramp.

states to be uniform, the dual-state boundary condition formulation could then be used to model a reduced simulation domain, in this case spherical for simplicity. By omitting the ramp wall in the simulation domain, computational domain was minimised. A comparison of the simulation domain from Butler et al (2021) and the reduced simulation domain is illustrated in figure 4.

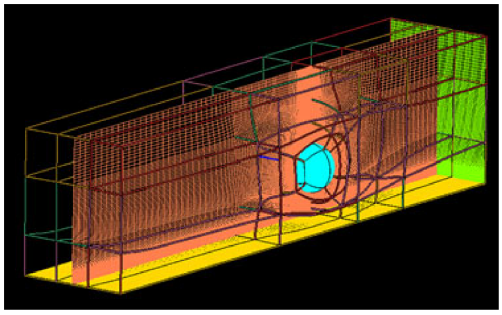

(a) Simulation domain utilised in Butler et al (2021).

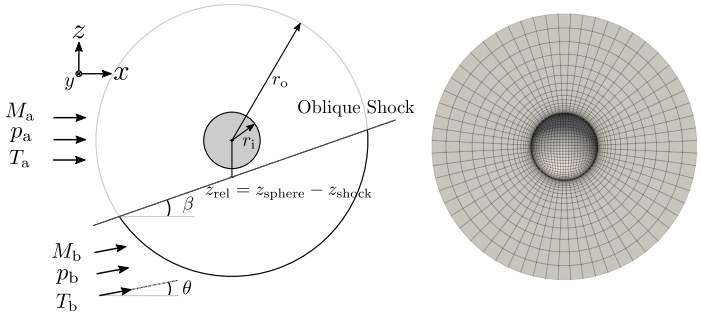

(b) Reduced sphere-ramp simulation domain with section view of computational mesh (every fourth cell shown for clarity).

Figure 4. Comparison of computational approaches. An oblique shock of angle β is generated from supersonic free-stream conditions (Mach number, pressure and temperature $M_\infty, p_\infty, T_\infty$) over a ramp with angle θ.

In the approach outlined in figure 4(b), both the free-stream and shock processed states were assumed to be uniform. The Rankine-Hugoniote relations outlined in equation (4) were solved iteratively to calculate the shock processed flow properties (state B).

$$\tan\theta = 2\cot\beta \frac{M_a^2 \sin^2\beta - 1}{M_a^2(\gamma + \cos 2\beta) + 2} \qquad M_b = \frac{1}{\sin(\beta - \theta)} \left(\frac{1 + \left(\frac{\gamma-1}{2}\right) M_a^2 \sin^2\beta}{\gamma M_a^2 \sin^2\beta - \left(\frac{\gamma-1}{2}\right)} \right)^{0.5} \tag{4}$$

4 Numerical Approach

The simulation domain was discretised into a structured, cartesian mesh, as illustrated in figure 4(b). Cells were clustered towards the sphere surface. A symmetrical mesh was generated to allow for global mesh movements during the two-way coupled trajectory simulations. The outer mesh surface employed the dual-state boundary condition, while a fixed temperature wall (with shear) boundary condition was applied to the inner spherical surface. A sphere wall temperature of 300K was chosen to represent laboratory conditions.

4.1 Fluid Solver

The fluid dynamics simulations were conducted using the Eilmer transient, compressible flow simulation program. The solver uses a cell centred finite volume formulation to solve the Reynolds Averaged Navier Stokes (RANS) equations, and is based on the AUSMV family of flux calculators (Wada & Liou (1994)). The formulation is detailed in equation (5).

$$\frac{\partial}{\partial t}\int_V \boldsymbol{U}\, dV = -\oint_S (\boldsymbol{F}_i - \boldsymbol{F}_v)\cdot\hat{\boldsymbol{n}}\, dA + \int_V \boldsymbol{Q}\, dV \tag{5}$$

Where $\boldsymbol{U}$ is the vector of conserved quantities (mass, momentum and energy), $\boldsymbol{F}_i$, $\boldsymbol{F}_v$ are the inviscid and viscous interface fluxes, $\boldsymbol{Q}$ is the source term vector and $\hat{\boldsymbol{n}}$ is the interface normal vector. The gas dynamics were marched in time using an Euler based predictor-corrector method, where a global time-step was determined by the CFL criterion. A maximum CFL number of 0.3 was enforced.

For simulations with two-way coupling, velocities for cell vertices over the entire domain were assigned based on the sphere dynamics. To account for the moving interfaces, a flux correction was applied. Taking an interface velocity (w_{if}), the corrective inviscid flux vector is formulated using the *relative* velocity $(\tilde{\boldsymbol{u}} - w_{if})$. A source term is then added to account for the work done on the fluid due to movement of the wall. The stability based on the maximum movement of each cell for a given time-step was considered, however the cell velocities relative to fluid velocities were found to be small enough to alleviate this concern.

Simulations were completed in parallel, using the Fawkes High Performance Computing (HPC) cluster at the University of Southern Queensland. The majority of simulations were completed using 81 CPUs and 200GB of memory, with wall clock times ranging from 1 hour to $\sim$ 4 days.

4.1.1 Mesh Independence

A mesh refinement study was completed to ensure the sufficient resolution of flow features relevant to the sphere dynamics. The study was completed in accordance with Roache (1998) and Stern et al (2001), with four grid refinements chosen, coarse, medium, fine and ultra-fine. Grids were refined by increasing the number of cells along each axis of the parametrised mesh. While care was taken to minimise the y^+ parameter for cells adjacent to the sphere wall, a strict limit of $y^+ < 1$ for all cells was not enforced. Viscous forces accounted for approximately 1% of the total force on the sphere, suggesting the thickness of cells normal to the wall should have a small effect on the total force.

Each grid was solved for flow conditions representing Mach 6 inflow over a 10° sharp ramp with $z_{rel} = 0$, and the impact of mesh refinement on the integrated forces over the sphere surface was observed. Results from the study are outlined in table 1.

Mesh	No. Cells	F_x (N)	ΔF_x (%)	F_z (N)	ΔF_z (%)	CPU Hours
Coarse	28,350	12.26	-	4.52	-	5.6
Medium	226,800	12.27	0.1	4.58	1.3	194.5
Fine	765,450	12.19	-0.7	4.54	-0.9	3,683.9
Ultra-Fine	1,814,400	12.14	-0.4	4.50	-0.9	5,850.1
Butler et al (2021)	-	12.00	-	4.20	-	-

Table 1. Mesh independency study results.

Results from table 1 suggest flow features in the coarse mesh weren't resolved in sufficient detail. Taking the medium, fine and ultra-fine grids, F_x appears largely independent of the grid spacing and displayed asymptotic convergence. F_z did not converge asymptotically, displaying a 0.9% change from both the medium to fine and fine to ultra-fine grids. As the reduced flow domain approach introduces a number of potential sources for numerical error, further work is needed to analyse the cause of these errors and improve convergence.

Although complete convergence was not displayed, a maximum deviation of 2.3% for F_x and 9.0% for F_z compared to Butler et al (2021) was observed across all grids. This close matching of results to literature gave confidence that the aim of this paper could be met using the reduced flow domain approach. That is, it was assumed the accuracy of these results was sufficient to report on

the development and application of the reduced flow domain approach to FSI problems. Keeping this goal in mind (and the computational costs), the medium resolution mesh was chosen for the remainder of this research. Future work will investigate and address the cause for non-convergence in detail.

4.2 One-way Coupled Sphere Dynamics Model

The aerodynamic forces were obtained through post-processing results from the fluid solver. These forces were then used as the basis for both a force and moment balance, used to define a sphere dynamics model. Assuming the sphere is a rigid body of uniform material, the force and moment balances about the sphere centre of gravity were formulated as:

$$\ddot{\boldsymbol{x}} = \sum \boldsymbol{F}/m \approx (F_x/m,\ 0,\ F_z/m - g) \qquad \ddot{\boldsymbol{\theta}} = \sum \boldsymbol{M}/I \approx (0,\ 0,\ 0) \tag{6}$$

Where the mass $m = (4/3)\pi r_i^3 \rho$ for a sphere with material density ρ. The force contributions in the y direction were observed to cancel due to symmetry, and the moment effects on the sphere were small relative to the linear acceleration and therefore omitted. The effect of these assumptions on the trajectory are highlighted in later sections. The forces were then normalised by the free-stream dynamic pressure $q_\infty = (1/2)\rho_\infty V_\infty^2$ and sphere cross sectional area A_{ref} to achieve the final dynamics model. The final dynamics model and force coefficients are outlined in equation (7).

$$\begin{pmatrix} F_x & F_z \end{pmatrix}^{\mathrm{T}} = q_\infty A_{ref} \begin{pmatrix} C_x & C_z \end{pmatrix}^{\mathrm{T}} = q_\infty A_{ref} \begin{pmatrix} C_D(M,\ x,\ z) & C_L(M,\ x,\ z) \end{pmatrix}^{\mathrm{T}} \tag{7}$$

$$\boldsymbol{x} = \begin{pmatrix} x & z & \dot{x} & \dot{z} \end{pmatrix}^{\mathrm{T}} \qquad \dot{\boldsymbol{x}} = \begin{pmatrix} \dot{x} & \dot{z} & \frac{q_\infty A_{ref}}{m} C_D(M,\ x,\ z) & \frac{q_\infty A_{ref}}{m} C_L(M,\ x,\ z) - g \end{pmatrix}^{\mathrm{T}} \tag{8}$$

Where C_D, C_L were taken as functions of the inflow Mach number M and sphere position relative to the shock. To simulate a sphere trajectory, the system in equation (8) was integrated using the well established Runge-Kutta 4th order integration technique, with the force coefficients linearly interpolated from a table at each time-step. As the present study is concerned with the body separation dynamics, the trajectory time-scales were small and the sphere velocity small compared to the inflow, allowing for a constant Mach number assumption over each trajectory.

4.3 Two-way Coupled Sphere Dynamics Model

The two-way coupled simulations made use of the moving mesh capability within the Eilmer code base. Aerodynamic forces were calculated at each time-step of the fluid solver, coupled to a six degree of freedom rigid body, uniform density sphere dynamics model. Each time-step, the dual-state boundary condition was used to update the flow field, which then informed the sphere dynamics and mesh movements. The dynamics model was formulated similarly to the one-way coupled sphere dynamics model, and included the effects of moments. The formulation is shown in equation (9).

$$\begin{pmatrix} \ddot{x} & \ddot{y} & \ddot{z} \end{pmatrix} = \begin{pmatrix} F_x/m & F_y/m & F_z/m - g \end{pmatrix} \qquad \begin{pmatrix} \ddot{\theta}_x & \ddot{\theta}_y & \ddot{\theta}_z \end{pmatrix} = \begin{pmatrix} M_x/I & M_y/I & M_z/I \end{pmatrix} \tag{9}$$

A material density of $\rho = 7700$ kg/m^3 was used for each two-way coupled simulation, and the moment of inertia was taken as $I = (2/5)mr_i^2$, with the sphere mass calculated previously. Both the translational and rotational accelerations were integrated using a first order forward Euler method. As CFL constraints enforced a maximum time-step of approximately dt $= 10^{-8}$ seconds, first order accuracy of the Euler integration was deemed acceptable. No structural deformation of the sphere surface was included in the coupled dynamics model.

5 Results and Discussion

Flow-fields from the fluid solver were examined to ensure the correct macroscopic flow features were captured. Results for $z_{rel}/r_i = 0$ are illustrated in figure 5, where the interaction between the oblique incident shock and the sphere bow shock is clearly captured in both the numerical schlieren and the density flow-field. The shock-shock interaction exhibits a clear triple point and impinges on the sphere surface, causing a high density and pressure region on the sphere underside. The high pressure region appears to be the primary factor for lift acting on the sphere, and is in good agreement with results from literature (Butler et al (2021)). As such, it was concluded that the dual-state boundary condition is capable of sufficiently resolving the macroscopic flow features using the reduced simulation domain. The fluid solver was then applied to both trajectory models, with trajectory results and the forces from 13 quasi-steady and 2 moving mesh fluid simulations provided in figure 6.

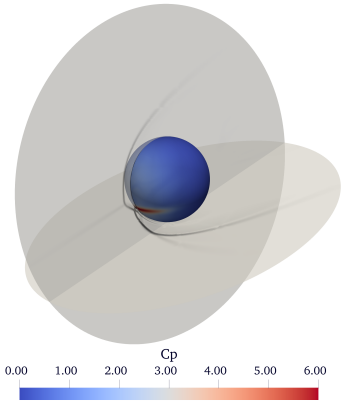

(a) Numerical Schlieren flow-field visualisation (fine mesh).

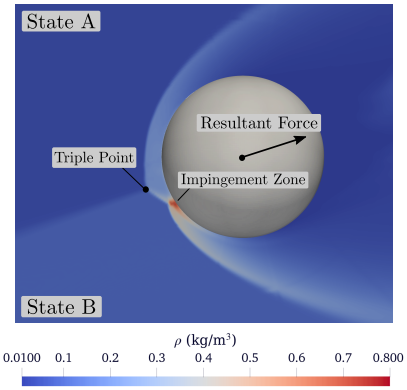

(b) Density flow-field illustration on X-Z plane (fine mesh).

Figure 5. Qualitative flowfield visualisation demonstrating the incident shock boundary condition for Mach 6 flow over a 10° ramp with the sphere centre directly intersecting the shock plane.

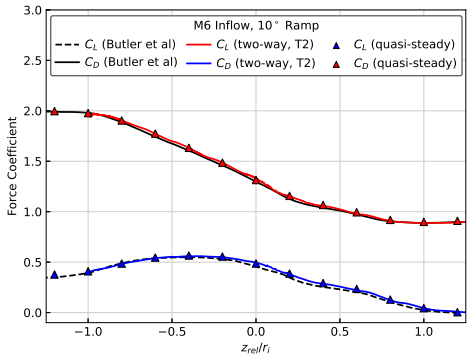

(a) Aerodynamic force coefficients from a two-way coupled simulation (trajectory 2 outlined in (b)) and 13 quasi steady fluid simulations for Mach 6 flow over a 10° ramp. A comparison to results in Butler et al (2021) is provided.

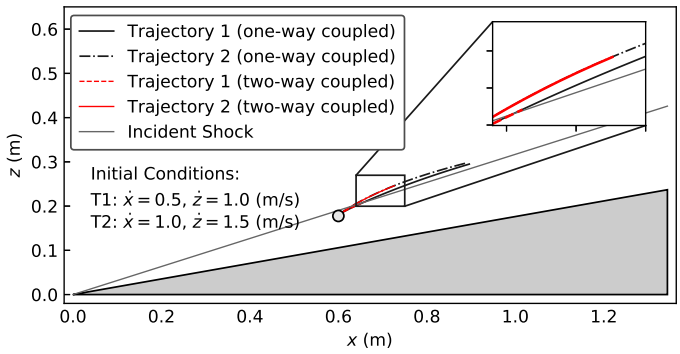

(b) Comparison of one-way and two-way trajectory calculations. One-way coupled trajectories were simulated for a 50ms, while the two-way trajectories (T1, T2) were simulated for 20ms and 30ms respectively with initial conditions outlined above.

Figure 6. The dual-state boundary condition applied both trajectory models.

The aerodynamic force coefficients from all quasi-steady simulations are in good agreement with literature (Butler et al (2021)), and a maximum difference of $\Delta C_L = 0.04$ was observed. Force coefficients from the two-way coupled simulation are also in good agreement with Butler et al (2021), however a small over-prediction in lift from z_{rel}/r_i = -0.1 to 1.0 was observed. A possible cause for this discrepancy is the two-way model coupling. As changes in the inflow propagate downstream from the mesh boundary, these changes take some small Δt to reach the sphere surface and affect dynamics. This delay introduces some error to the dynamics model, likely proportional to the sphere velocity,

however further work is needed to characterise this error. Model error introduced in the formulation of the dual-state boundary condition is also a possibility. The one-way trajectory model will be well suited for future Monte Carlo applications to investigate this uncertainty propagation downstream.

From figure 6(b), trajectories from the one-way and two-way coupled models are in great agreement. For the sphere-ramp problem, this suggests the effect of moments and velocity on the sphere dynamics are minimal. However, as this approach will be applied to irregular objects in future, their accurate modelling is important. While the two trajectories compared in figure 6(b) suggest the reduced flow domain approach can effectively model the dynamics of objects with hypersonic FSI, further work is recommended in classifying the accuracy and region of applicability.

6 Conclusions

In this work, a dual state boundary condition to model hypersonic FSI using a reduced flow domain was formulated, and implemented in the Eilmer compressible flow CFD program. The approach was then applied to one-way and two-way coupled trajectory simulations of a sphere-ramp problem recently solved in literature. The fluid solver resolved the macroscopic flow features well, and aerodynamic force coefficients measured from both static and moving mesh simulations showed good agreement with literature, confirming the suitability for such an approach. While further work is required to ensure accuracy for future problems, this work validated the reduced flow domain approach for a simple space debris dispersion problem, and further studies are planned. Future work will include investigating more complex incident flow-fields, irregular bodies and the use of such models for propagating uncertainty for downstream trajectories.

Acknowledgements

This research was supported under the Australian Research Council's Discovery Project funding scheme (Project DP220102751 - Dispersion of Spacecraft Components During Re-entry). Aspects of this work were also supported by the Australian Government Research Training Program.

References

NASA, NASA Orbital Debris Quarterly News, Q2 2022, NASA Orbital Debris Program Office.

Laurence, S.J., and Deiterding, R., Shock-wave surfing, 2011, in *Journal of Fluid Mechanics*, vol 676. (10.1017/jfm.2011.57)

Reyhanoglu, M. and Juan A. Estimation of debris dispersion due to a space vehicle breakup during reentry, in *Acta Astronautica*, 86, 211-218. (10.1016/j.actaastro.2013.01.018)

Butler, C.S., Whalen, T.J., Sousa, C.E. and Laurence, S.J., Dynamics of a spherical body shedding from a hypersonic ramp. Part 2. Viscous flow, 2021, in *Journal of Fluid Mechanics*, vol 906. (10.1017/jfm.2020.757)

Gibbons, N. and Damm, K. and Jacobs, P. and Gollan, R. J. Eilmer: an Open-Source Multi-Physics Hypersonic Flow Solver, 2022, Preprint in *arXiv*. (10.48550/ARXIV.2206.01386)

Jacobs, P. A. and Gollan, R. J. (2016) Implementation of a Compressible-Flow Simulation Code in the D Programming Language, Applied Mechanics and Materials, vol 846, pp. 54-60.

Wada, Y. and Liou, M. S., A flux splitting scheme with high-resolution and robustness for discontinuities, AIAA Paper 94-0083, 1994

Roache, P.J. Verification and Validation in Computational Science and Engineering. 1998, *Hermosa Publishers*, Alburquerque, New Mexico.

Stern, F., Wilson, R., Coleman, H. and Paterson, E. Comprehensive Approach to Verification and Validation of CFD Simulations-Part 1: Methodology and Procedures, 2001, in *Journal of Fluids Engineering*, vol 123.

Boley, A.C., Byers, M. Satellite mega-constellations create risks in Low Earth Orbit, the atmosphere and on Earth. *Sci Rep 11*, 10642 (2021). (10.1038/s41598-021-89909-7)